Research Paper

Numerical and Experimental Analysis of Geometric Patterns in FDM-printed PCL Bone Scaffolds

Hosein Rostamani[1], Omid Fakhraei[2*], Hediye Paranion[2], Anahita Mousazadeh Moghaddam[2], Mohammad Javad Khosravi[2]

1. Department of Biomedical Engineering, School of Biomedical Engineering, Amirkabir University of Technology (Tehran Polytechnic), Tehran, Iran.
2. Department of Biomedical Engineering, Ma.C., Islamic Azad University, Mashhad, Iran.

Use your device to scan and read the article online

Citation Rostamani H, Fakhraei O, Paranion H, Mousazadeh Moghaddam A, Khosravi MJ. Numerical and Experimental Analysis of Geometric Patterns in FDM-printed PCL Bone Scaffolds. Journal of Translational Regenerative Medicine. 2025; 1:E1019. http://dx.doi.org/10.32598/JTRM.1.1019

http://dx.doi.org/10.32598/JTRM.1.1019

ABSTRACT

Background: In this study, three-dimensional (3D)-printed polycaprolactone (PCL) scaffolds were fabricated using the fused deposition modeling (FDM) technique with different geometric patterns and underwent finite element analysis under tensile, compressive, and bending loadings, along with experimental testing.

Methods: The 3D models of six scaffolds were designed in SolidWorks software. Scaffolds No. 1, 2, 3, 5, and 6 had a disk geometry with a diameter of 4 cm, while scaffold No. 4 was square-shaped with a side length of 3 cm. Their cross-sectional thickness and overall height were kept constant; differences pertained exclusively to pore geometry and pore arrangement. They underwent numerical study using von Mises stress, displacements (URES), and equivalent strain (ESTRN) maps, and were validated against experimental results. The surface morphology and fracture characteristics were examined using scanning electron microscopy (SEM) images.

Results: Scaffold No. 5 was the most efficient model and was selected as the optimal pattern. The SEM image of this optimal scaffold confirmed the geometric regularity of the cylindrical pore arrangement and the characteristic layer-by-layer filament deposition of the FDM process, while post-tensile fracture SEM imaging revealed interlayer separation and polymer features consistent with the ductile nature of PCLs. The optimal scaffold with straight cylindrical pores provided lower displacement and more uniform stress/strain distribution compared to the one with conical pores, while the addition of a symmetric protrusion on the opposite face of the scaffold did not yield a significant mechanical benefit.

Conclusion: The findings underscore the decisive role of geometry and pore configuration in tuning the mechanical microenvironment of PCL scaffolds for tissue engineering applications.

Keywords: Three-dimensional (3D) printing, Polycaprolactone (PCL), Microstructure, Tissue engineering, Simulation

Article info:
Received: 12 Jun 2026
Accepted: 08 Jul 2026
Publish: 03 Aug 2026

*** Corresponding Author:**
Omid Fakhraei, Assistant Professor.
Address: *Department of Biomedical Engineering, Ma.C., Islamic Azad University, Mashhad, Iran.*
Phone: *+98 (936) 1351735*
E-mail: *omid.fakhraei@iau.ac.ir*

Highlights

- The study establishes a practical design framework for zone-matched PCL scaffolds and recommends incorporating geometric nonlinearity and cyclic fatigue testing as next steps toward clinical translation.

- Compared to bilateral and conical configurations, unilateral cylindrical pores produced more uniform displacement fields, lower peak deflection, and reduced stress concentration at inter-pore bridges.

- Numerical and experimental tests confirmed that localized refinements are sufficient to enhance the structural performance of scaffolds without changing the fundamental pore geometry.

- Bilateral and conical configurations introduced stress concentration bands and reduced the effective moment of inertia, offering no meaningful gain in stiffness or peak stress reduction compared to the unilateral cylindrical design.

Plain Language Summary

Every year, many people need bone repair after an injury, an infection, or surgery to remove diseased tissue. Surgeons often need something to fill the gap. One promising option is a scaffold: a small, porous structure that works as a temporary framework, holding the space open and supporting the body's own cells while new tissue grows in and the scaffold slowly breaks down. A scaffold has to be stiff enough to carry the loads the body puts on it but also full of open channels so that cells, nutrients, and fluids can move through. Striking that balance depends heavily on the shape and arrangement of the holes inside it. In this study, we three-dimensional (3D)-printed scaffolds from polycaprolactone, a medically approved plastic that degrades slowly and safely inside the body, using six different patterns. Each design was tested twice: first in computer simulations that predicted how it would squash, stretch, and bend, and then in the laboratory, where real printed samples were pulled apart in a mechanical testing machine. A high-powered microscope was used to inspect the printed surfaces and the broken edges. The computer predictions and the laboratory measurements broadly agreed on which designs performed best. The best performer used evenly spaced, straight cylindrical holes opening on one side only; it spread the load smoothly across the whole structure instead of concentrating it at a few weak points. Cone-shaped holes, which narrow toward one end, and holes with matching bumps on both faces made the scaffold weaker rather than stronger while being harder to print. The practical message is that a scaffold's mechanical behavior can be tuned simply by redesigning its internal geometry, without costly additives. Biological testing and long-term durability studies remain necessary next steps.

Introduction

Each year, a significant number of patients require bone grafting due to lesions and complications of skeletal injuries. Depending on the nature of these injuries, different therapeutic approaches are used to manage bone defects. One approach is the use of tissue implants. Tissue engineering is a popular branch of regenerative engineering that contributes to healthcare by substituting damaged tissue with prostheses fabricated by various methods [1]. It has been recognized as a reliable approach to addressing tissue injuries by mimicking the physiological environment. It draws upon the principles of medicine, biology, and engineering, integrating them in the design of biological substitutes to restore, maintain, and enhance tissue function [2]. Bone tissue engineering typically involves the use of three-dimensional (3D) scaffolds to establish a suitable environment for cell proliferation and the regeneration of damaged tissues or organs [3].

Tissue engineering scaffolds should exhibit biocompatibility, adequate porosity, bioactivity, biodegradability, and favorable physical and mechanical properties, and be able to facilitate cell adhesion. The scaffold properties can be tailored by selecting an appropriate fabrication technique [4]. Scaffold fabrication techniques, along with material selection, play a critical role in determining scaffold properties for targeted applications. Various strategies exist for scaffold fabrication, including electrospinning, freeze-drying, solvent casting, and 3D printing techniques [4, 5]. Scaffolds fabricated via 3D printing (additive manufacturing) are widely used in bone tissue engineering due to their free design selection, precise control over geometry and interconnectivity, and high reproducibility. Furthermore, this approach allows optimization of desired mechanical properties by modifying printing patterns.

A broad range of polymeric (natural and synthetic), ceramic, and composite materials has been investigated for the fabrication of tissue engineering scaffolds. However, synthetic polymeric materials remain the most commonly used for scaffold fabrication due to their low immunogenicity and cytotoxicity, ease of processing, and tunable properties during polymer synthesis [6]. Biodegradable polymers play a fundamental role in tissue engineering. Using various technologies, researchers have successfully fabricated 3D tissue engineering scaffolds from these polymers. These scaffolds serve as temporary templates, providing physical and biochemical signals to cells, and ultimately determining the successful outcome of tissue regeneration [7]. Polycaprolactone (PCL) is among the most relevant synthetic polymers and has been investigated for bone scaffold applications due to its excellent mechanical properties and biocompatibility in supporting cell growth and differentiation, the processes that can ultimately lead to bone tissue regeneration [6]. PCL is also widely employed in long-term surgical implants and slow-release drug delivery systems [8]. It is a semicrystalline biodegradable polyester with a low melting point. This polymer exhibits superior viscoelastic properties and can be processed at lower temperatures compared to other polymers. It also imparts favorable mechanical properties to printed structures [5, 9]. PCL possesses characteristics such as biocompatibility, a slow degradation rate, reduced acidic degradation byproducts, and load-bearing potential compared with other polyesters, and has been widely used as a promising biomaterial for tissue engineering applications. Nevertheless, the hydrophobic nature of PCL limits its applicability in tissue engineering [3, 9–12].

In the present study, PCL-based scaffolds were fabricated by 3D printing in six distinct patterns. Subsequently, to evaluate and compare the mechanical behavior of each pattern, load application simulations as well as tensile mechanical testing and scanning electron microscopy (SEM) were used in order to identify the optimal scaffolds.

Materials and Methods

Fabrication of PCL scaffolds

Pure PCL scaffolds were fabricated using the fused deposition modeling (FDM) technique. Initially, a 3D model of the scaffold was designed in SolidWorks software, version 21. PCL was annealed at temperatures ranging from 60 to 80 ˚C for 2-4 hours to improve mechanical properties and interlayer adhesion. High-molecular-weight PCL (>40,000 g/mol) was selected. The polymer was subsequently extruded into filament form to render it compatible with FDM printing. Scaffolds were printed in a layer-by-layer manner and separated from the build plate upon completion. Scaffolds No. 1, 2, 3, 5, and 6 were fabricated in a disk geometry with a diameter of 4 cm, while scaffold No. 4 was square-shaped with a side length of 3 cm. Cross-sectional thickness and overall height were kept constant across all scaffolds; differences pertained exclusively to pore geometry and pore arrangement.

Load application simulation

To predict mechanical response prior to physical testing, numerical simulations were performed in SolidWorks Simulation (Static module) on the CAD models of the scaffolds. The material was assumed to be linearly elastic and isotropic. Initial values of Young's modulus (E) and Poisson's ratio (ν) were obtained from the literature and subsequently calibrated against tensile test results. Meshing was carried out using second-order tetrahedral elements via a curvature-based approach and verified through a convergence study (stiffness variation <5%), where internal contacts were defined as bonded.

A linear elastic, small-deformation formulation was adopted as the primary analytical framework because the goal of the simulation was a comparative, geometry-based screening of six pore architectures under identical loading and boundary conditions, rather than absolute failure-load prediction. This allows direct, computationally efficient comparison of stiffness, load-path continuity, and the relative location and severity of stress concentrations across different patterns under a common set of constitutive assumptions. A priori knowledge indicates that, given the relatively low yield strength of PCL (≈5 MPa) and the magnitude of the applied loads (set to match experimentally measured peak fracture forces), computed Von Mises stresses in several regions and patterns exceed this threshold. In such cases, the reported stress values and associated factors of safety are interpreted as relative, qualitative indicators of risk and ranking among designs rather than quantitatively accurate predictions of the true post-yield stress field, which would require an elastoplastic or hyperelastic constitutive model combined with a geometrically nonlinear (large-displacement) formulation.

Loading conditions were quasi-static and displacement-controlled, encompassing axial tension (with a numerical gauge length of L_0=150 mm), axial compression, and three-point bending with a span consistent with the laboratory configuration. One end of the specimen was fully constrained, while a Remote Displacement boundary condition was applied at the opposite end. Contact with rigid supports was modeled as non-penetrating, and the large-deformation option was activated when necessary. Outputs including force–displacement and stress–strain curves, Von Mises stress maps, and principal strains were extracted and compared against physical tensile test results (crosshead speed: 5 mm/min, L_0=150 mm) for validation purposes.

Applied loads differed across the six patterns because each simulation was driven to the experimentally measured peak fracture force of the corresponding specimen group, so that the predicted stress field corresponds to the actual physical condition under which each scaffold failed during testing rather than an arbitrary common load. Since the model was linear elastic, the computed stress scale was proportional to the applied force; therefore, effective stiffness ($k=F/\delta$) was load-independent and directly comparable across patterns, while peak stress was also reported in normalized form ($\sigma max/F$) to enable a load-independent, geometry-driven comparison of stress concentration severity.

Tensile testing

The 3D printed scaffolds were prepared for axial tensile testing following dimensional inspection. A total of six independent groups of specimens were prepared, with three scaffolds tested as replicates per group (n=18). Testing was conducted using a universal testing machine. The specimens were gripped in the machine jaws, and the initial gauge length (L_0) was set at 150 mm. Jaw displacement was applied at a constant crosshead speed of 5 mm/min until fracture, and force–displacement data were recorded continuously. The effective width and thickness of each specimen were measured at multiple points using a digital caliper and averaged to calculate the cross-sectional area, thereby enabling conversion of force and displacement data into stress and strain. From the resulting stress–strain curves, Young's modulus (slope of the elastic region), ultimate tensile strength, and fracture strain were extracted. The results for each group were reported as Mean±SD. All tests were conducted under stable laboratory conditions with prior instrument calibration. Statistical comparisons among the six scaffold patterns were performed using one-way ANOVA followed by Tukey's post-hoc test in GraphPad Prism software, version 10.1.2, with a significance level set at 0.05.

Scanning electron microscopy

The surface morphology and fracture characteristics of the optimum scaffold were examined using an SEM device (MIRA3 TESCAN) at an accelerating voltage of 20.0 kV with a secondary electron (SE) detector. Two imaging conditions were employed: surface imaging of the as-printed scaffold to assess pore geometry and filament deposition quality, and cross-sectional imaging of the fracture surface following tensile testing to characterize the failure morphology. Prior to imaging, specimens were mounted on aluminum stubs and sputter-coated with a thin conductive layer to prevent charge accumulation. Surface micrographs were acquired at magnifications of ×12 and ×20 (view fields of 12.0 mm and 6.92 mm, respectively), and fracture surface micrographs were obtained at ×25 and ×1500 magnifications (view fields of 5.54 mm and 92.3 µm, respectively).

Results

3D printing of PCL scaffolds with different geometric patterns

The scaffolds with six different geometric patterns, fabricated from PCL filaments using the FDM technique, are shown in Figure 1. The models were fabricated in a circular geometry with identical dimensions to enable a comparative assessment of the influence of various patterns on scaffold properties, except for scaffold No. 4, which was non-circular as a control specimen. The models were subsequently saved in STL format and then converted to G-code format for transfer to the 3D printer, rendering them readable by the machine. The mechanical properties of printed PCL specimens are primarily governed by process parameters and architectural design, and the incorporation of dyes or fluorophores at low concentrations does not result in any significant mechanical deterioration; therefore, the effect of colorants present in the PCL filaments was considered negligible [13, 14].

Simulation of scaffolds' compressive behaviors

In simulating the compressive behavior of specimen No. 1, a porous disk with a triangular pattern was fully constrained at the base, and a distributed compressive load of F=417.3 N was applied from the top. The resultant displacement plot (URES) showed structural shortening with a maximum of approximately 11–12 mm in the upper loaded region, with displacement values decreasing uniformly toward the support. The deformed shape rendered at a deformation scale of approximately 0.35 was presented for illustrative purposes only, and actual values were read directly from the legend (Figure 2). In the Von Mises stress map, a maximum stress of $\sigma_v M \approx 1.31\times10^8$ Pa was predominantly observed along the upper outer ring and around the triangle vertices aligned with the loading direction. Secondary stress concentrations were also present at the lower support. The maximum effective/principal strain was reported at approximately $\varepsilon_{max} \approx 0.83$, indicating large localized deformations in the load-bearing regions. Given the designated yield strength of 5.0×10^6 Pa, considerable portions of the structure exceeded the yield limit, suggesting that local plastic yielding or damage is likely to occur at this load level. It should be noted that no contact interactions were defined in the current model (Number of Contacts=0); therefore, support behavior was modeled as full constraints, and contact or sliding effects were not incorporated into the simulation, which may influence stress concentration predictions at the boundaries.

Regarding discretization, the model comprised 68,188 elements and 114,307 nodes, with 338,277 degrees of freedom and a total solution time of approximately 5 seconds. However, an "excessive displacements" warning was recorded in the solver log, accompanied by a recommendation to activate the Large Displacement option. In the analysis, the solution was continued under the Small Displacement assumption. For improved accuracy, particularly given the large strains and appreciable geometric deformation observed, it is recommended that the analysis be repeated with geometric nonlinearity (Large Displacement formulation) and, where feasible, an elastoplastic material model. Additionally, local mesh refinement around the triangle corners and the peripheral ring through h-adaptive or curvature-based approaches would yield more stable stress concentration estimates at sharp features. These findings are consistent with previously identified design considerations, namely: reinforcement or thickening of the peripheral ring, application of fillets to triangle corners, reduction of pore spacing in the vicinity of loading and support regions, and enhancement of material strength where possible. For a numerical report of effective stiffness, it is recommended that the stiffness be computed as $k=F/\delta$ from the support reaction force and the corresponding displacement. Where accessible, the reaction force–displacement curve should be extracted and presented.

In scaffold No. 2 (hexagonal lattice), a uniform compressive load of F=47.1 N was applied to the right semicircle while the left edge was fully constrained. The displacement map showed that the maximum displacement occurred in the loaded region and along the peripheral ring, with a value of approximately $\delta_{max} \approx 16.1$ mm, read from the color legend (Figure 2). Accordingly, the effective compressive stiffness of the structure ($k=F/\delta_{max}$) was estimated at $\approx 47.1/16.1 \approx 2.9$ N/mm, reflecting a more compliant response compared to scaffold No. 1. The strain field was more homogeneous than that of scaffold No. 1, though mild concentrations were observed along the load transfer path from the peripheral ring to the first row of cells. The deformation in this pattern was primarily governed by ring bending and boundary bracket flexure, while the contribution of the central cells to load bearing is comparatively minor. In the Von Mises stress maps, the highest stresses were observed at the ring–lattice junctions and along the cell edges adjacent to the load front, while a large portion of the hexagonal core remained within the blue-to-dark-green range. Given the designated yield strength of 5 MPa, the prevailing stresses in most regions remained below the yield threshold, with only localized patches near contact zones and edges approaching this limit. Mesh quality was uniform across all presented views, and adequate element density in the boundary regions enabled reliable capture of the stress and strain distribution patterns. In summary, under a constant compressive load, scaffold No. 2 exhibits greater displacement than scaffold No. 1 (i.e. lower stiffness); however, the more uniform stress distribution throughout the lattice prevented the formation of extensive critical zones, resulting in a safer overall response with respect to global yielding.

Under lateral compression (F=425.9 N), scaffold No. 3 (circular pores) developed a relatively uniform displacement gradient with $\delta_{max} \approx 37.8$ mm, yielding $k \approx 11.3$ N/mm, approximately 3.9 times stiffer than the scaffold No. 2 ($k \approx 2.9$ N/mm), with load transferred primarily through the inter-pore bearing ligaments while the peripheral ring suppressed global warping (Figure 2). Von Mises stress concentrations in these ligaments and near the support clearly exceeded the 5 MPa yield reference, necessitating a plasticity or softening formulation rather than a purely linear elastic model. Performance may be improved by widening the load-aligned ligaments, reducing pore diameter or density near the loaded region, thickening the outer boundary into a more continuous frame, and introducing fillets at pore junctions to relieve stress concentrations.

The compressive results for scaffold No. 4 under a load of F=275 N revealed a uniform global displacement gradient from the constrained edge toward the loaded

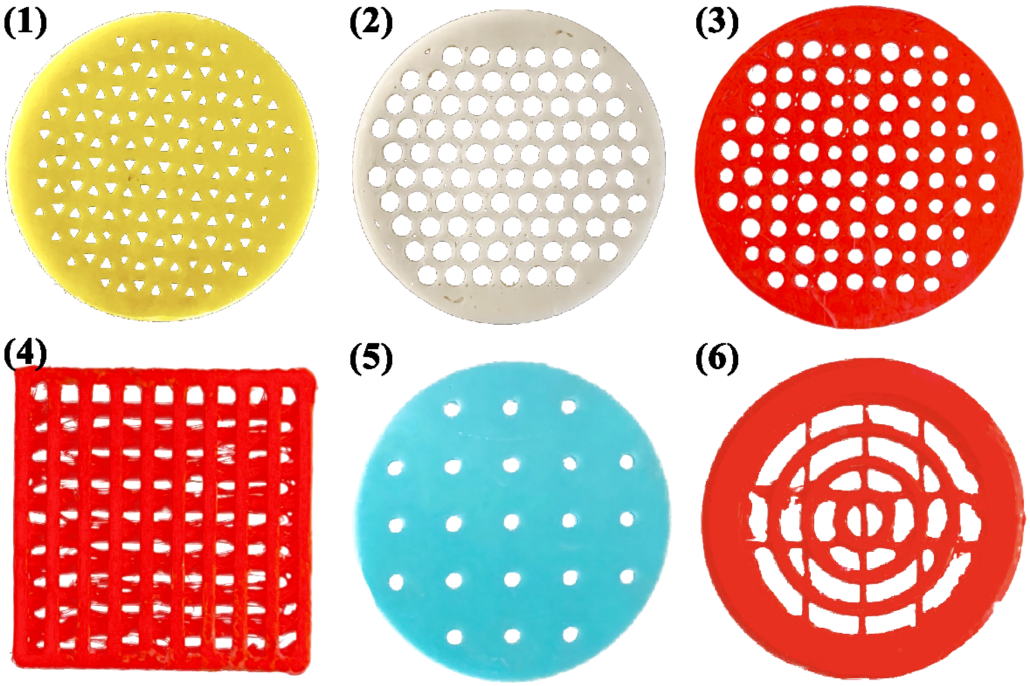

Figure 1. Images of 3D-printed PCL scaffolds in six geometric patterns, along with their numbers

Note: Disk-shaped scaffolds had a diameter of 4 cm, and the square-shaped scaffold had a side length of 3 cm.

edge (Figure 2), with $\delta_{max} \approx 6.6$ mm observed at the free edge, yielding an effective in-plane stiffness ($k=F/\delta$) of $\approx 275/6.6 \approx 41.7$ N/mm (compliance $C=\delta/F \approx 0.024$ mm/N). Stress and strain bands developed along the webs of the horizontal struts, which constitute the primary load-transfer path, while the contribution of the vertical struts was limited. The maximum Von Mises stress was observed at the intersections and along the loaded edge, reaching $\sigma_v M_{max} \approx 7.85\times10^7$ Pa, with the majority of struts falling within the range of approximately 1.5×10^7 to 3.5×10^7 Pa. The equivalent strain map also exhibited localized maxima at the inner corners of the square pores, with $\varepsilon_{eq,max} \approx 0.35$; these peaks are attributable to sharp corner effects and the relatively coarse mesh, and fracture assessment should therefore be based on average values across the strut webs, which are considerably lower. From a mechanical standpoint, the uniform URES gradient and stress bands along the horizontal struts indicated that the structural response under this loading was predominantly axial tension–compression along the horizontal struts, with no out-of-plane buckling or distortion observed. The load distribution along the plate height was approximately homogeneous, and the concentrations were primarily associated with the corner geometry. Two direct modifications are proposed to achieve incremental improvement without significant mass alteration: (i) rounding of the internal pore corners with a fillet radius of approximately $r \approx 0.5t$ to $1.0t$ to reduce stress concentration factors and stabilize stress and strain peaks; and (ii) reinforcement of the outer strut adjacent to the loaded edge by increasing its width by approximately 15-25% to reduce δ_{max} by several tenths of a millimeter and raise k to approximately 45–50 N/mm. Local mesh refinement at the internal corners is also recommended for more reliable estimation of σ and ε.

Under in-plane compression (F=548.7 N), scaffold No. 5 exhibited a uniform displacement gradient from the constrained left edge to the loaded right edge (Figure 2), with $\delta_{max} \approx 16.7$ mm, yielding $k \approx 33$ N/mm and $C \approx 3.0\times10^{-2}$ mm/N. Von Mises stress reached its peak at $\sigma max \approx 4.9\times10^7 N/m^2$ in the lateral-row pore collars and connecting ridges, giving a factor of safety (FoS) ≈ 0.10 relative to $\sigma_y \approx 5\times10^6 N/m^2$. Since local web buckling is likely to precede yielding, the allowable load should be restricted to 30–50 N, and load capacity may be improved by edge reinforcement, increased fillet and web thickness, anti-buckling beads, and distributed loading.

Scaffold No. 6 (F=187.2 N) developed a bowl-shaped deformation concentrated at the inner rings, with $\delta_{max} \approx 44.3$ mm, $k \approx 4.2$ N/mm, and $C \approx 0.237$ mm/N (Figure 2). The load was channeled through three radial struts to the inner rings, producing average strains of 0.1–0.3 along the struts and localized stress peaks on the order of 10^8 Pa at strut–ring junctions, yielding a local FoS ≈

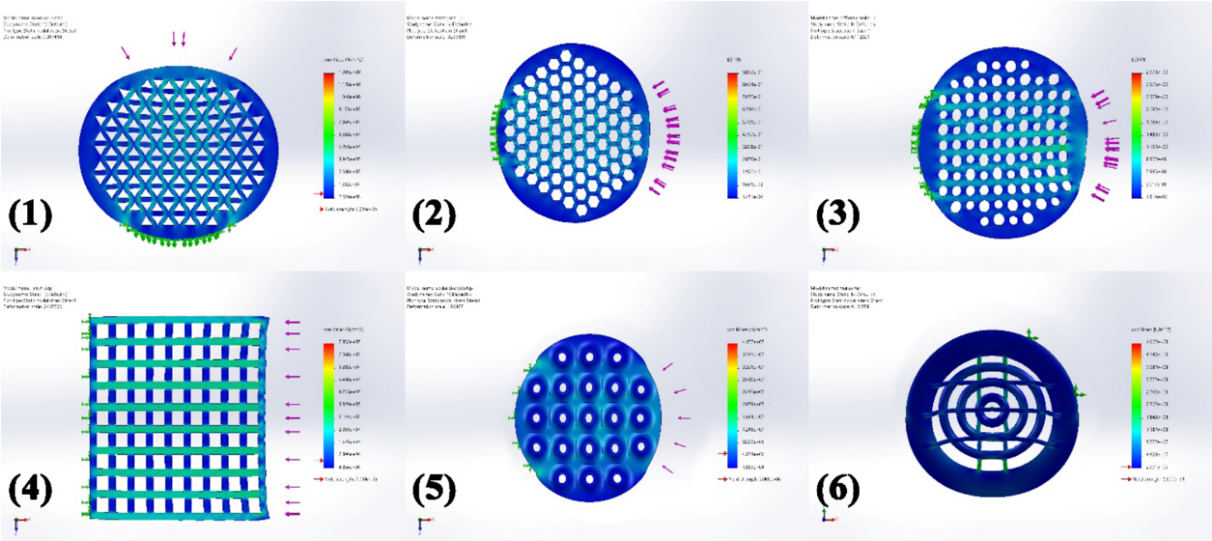

Figure 2. Simulation of the compressive behavior of six scaffolds with different geometric patterns in the simulation environment

0.06–0.12. Given numerical singularities at point supports, structural adequacy should be evaluated against average ring stresses (4×10^7–8×10^7 Pa) rather than peak values. To improve the compressive response at constant mass, the most effective interventions were evident from the stress and strain fields: (a) increasing the width/thickness of the two inner rings and the roots of the radial struts by 30–40% (redistributing material from the outer ring to the central regions); (b) introducing fillets at the strut-to-ring junctions to reduce stress concentration factors; and (c) adding a fourth radial strut (from three to four) or a narrow intermediate ring to distribute the load more uniformly. A reasonable quantitative target would be the reduction of the peak displacement to $\delta \approx 30$ mm, which can raise the stiffness to $k \approx 187.2/30 \approx 6.24$ N/mm while simultaneously reducing peak stresses (under the same load) by 20–35%.

The compressive stiffness ranking of scaffolds is as follows: scaffold 4 at $k \approx 41.7$ N/mm, scaffold 1 at ≈ 36 N/mm, scaffold 5 at ≈ 33 N/mm, scaffold 3 at ≈ 11.3 N/mm, scaffold 6 at ≈ 4.2, and scaffold 2 ≈ 2.9 N/mm. From a strength perspective, peak stresses in scaffold No. 1 reached approximately σmax ≈ 1.31×108 Pa (FoS ≈ σ_y/σ_{max} ≈ 0.04 with σ_y=5 MPa), and in scaffold No. 4, approximately 7.85×10^7 Pa (FoS ≈ 0.06); for pattern 5, approximately 4.9×10^7 Pa (FoS ≈ 0.10). For scaffold No. 3, stresses in the "tens of megapascals" range were all below a safety factor of 1. For scaffold No. 6, it was approximately (4–8)× 10^7 to 10^8 Pa depending on the region (FoS ≈ 0.06–0.12), while scaffold No. 2 remained predominantly below yield, with only localized patches near the edges approaching the threshold. Consequently, to maximize stiffness as the sole objective, pattern No. 4 is the optimal choice. If adequate stiffness combined with the potential to reduce stress peaks through localized geometric modifications is desired, pattern No. 5 offers the best compromise. If safety against yielding is the primary goal and larger displacements are acceptable, pattern No. 2 is the safer choice. Pattern No. 1, despite its high stiffness, requires substantial geometric and/or material improvements due to its extremely high stress concentrations.

Simulation of scaffolds' bending behaviors

In scaffold No. 1, loading was defined as a downward line force applied to the upper surface, with linear/point green constraints along one diameter serving as the support; therefore, the response represented quasi-three-point bending with a single bearing surface. The resultant displacement map (URES) exhibited the classical bending pattern with a maximum of $\delta_{max} \approx 14.1$ mm at the peripheral ring distal to the supports (the deformation scale of approximately 0.28 is for visualization purposes only). Accordingly, the effective bending stiffness ($k=F/\delta_{max}$) was ≈ 62.3/14.1 ≈ 4.4 N/mm. Furthermore, in the frontal and isometric views, a diagonal deformation/shear band was observed along the constraint line, indicating triangular load channeling and bending anisotropy (Figure 3). From a stress–strain perspective, Von Mises peaks were concentrated primarily at the peripheral ring on the loading side, at the junctions of the triangular webs with the ring, and around the sharp corners of the triangular features. The $\sigma_v M_{max}$ was ≈ (2.4–2.5) $\times10^7$ N/m² and ε_{max} was ≈ 0.14. Given $\sigma_y \approx 5\times10^6$ N/m², yielding

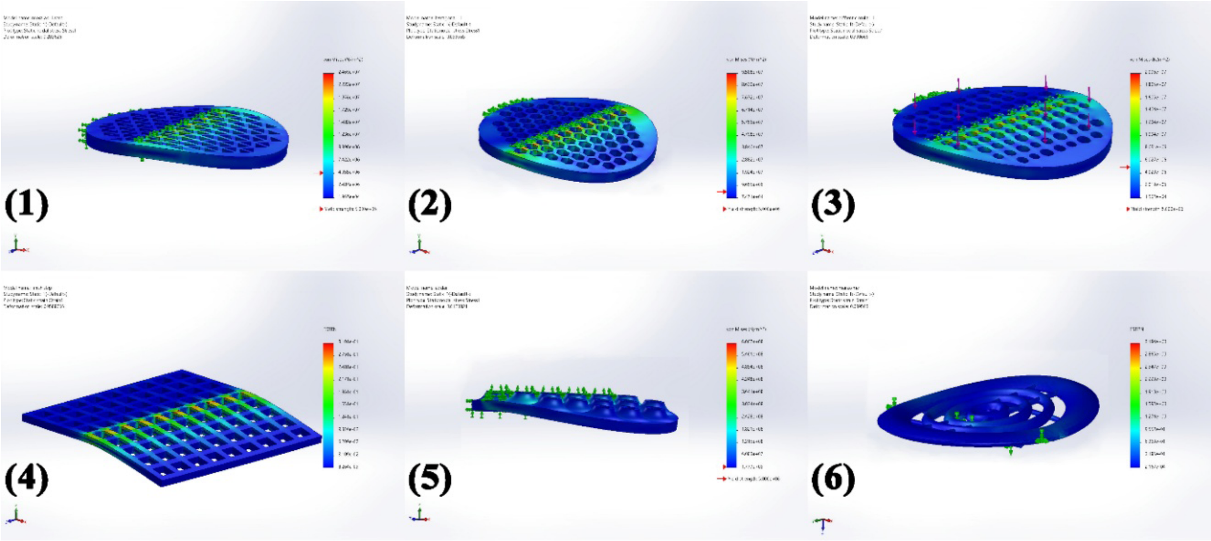

Figure 3. Simulation of the bending behavior of six scaffolds with different geometric patterns in the simulation environment

in these regions was possible. Accordingly, the following modifications are recommended to enhance bending stability: Application of fillets to the triangle corners, reinforcement and thickening of the peripheral ring, and increasing web width or reducing pore size in the vicinity of the load path and support regions. From a modeling standpoint, given the relatively high δ_{max}, activation of the Large Displacement formulation (geometric nonlinearity) is recommended, along with an elastoplastic material model where available, and local mesh refinement at the ring, corners, and support regions. Furthermore, if sliding contact is present in the physical experiment, replacing full constraints with frictionless non-penetrating contact can yield more realistic stress predictions.

The bending results for scaffold No. 4 under a total load of F=17.8 N showed that the maximum displacement occurred at the free edge, with a value of $\delta \approx 49.1$ mm according to the URES map (Figure 3). Accordingly, the effective stiffness ($k=F/\delta$) was $\approx 17.8/49.1 \approx 0.36$ N/mm, with a compliance ($C=\delta/F$) value of ≈ 2.7 mm/N. The uniform displacement gradient from the support to the free edge indicates that the structural response is predominantly global bending rather than localized deformation. The highest strains, and consequently the highest stresses, were concentrated in the outer ligaments of the terminal columns and along the tensile fibers near the loaded edge. This pattern reduces the effective moment of inertia in the loading direction due to the successive square pores, thereby amplifying δ. Low-cost strategies for increasing k include: Adding a peripheral frame or a continuous rail along the free edge, increasing the width of the last two rows of ligaments in the loading direction, and introducing fillets at the pore corners to mitigate stress concentration. A reasonable quantitative objective is to reduce δ to approximately 30–35 mm, which can raise k to approximately 0.5–0.6 N/mm.

Under bending, scaffold No. 5 (F=91.3 N) behaved analogously like a cantilever, with maximum displacement at the free right edge reaching $\delta_{max} \approx 348$ mm, giving $k \approx 0.26$ N/mm and $C \approx 3.8$ mm/N (Figure 3). Von Mises stress peaked at $\sigma max \approx 6.1\times10^{8}$ Pa in the protrusion bases and connection fillets within the critical shear–bending band, yielding FoS ≈ 0.008 and an allowable load (F_{allow}) of only ≈ 0.75 N, indicating that the response has exceeded the linear elastic range and requires geometric nonlinearity and plasticity to be properly captured. Redistributing material to the critical band, adding longitudinal ribs between the constrained strip and the first cell row, enlarging fillets, and spreading the load across multiple cells are recommended to bring the response toward elastic behavior, targeting δ in the tens-of-millimeters range and $k \approx 0.5$ N/mm.

Scaffold No. 6 (F=41.5 N, $\delta_{max} \approx 101$ mm) achieved $k \approx 0.41$ N/mm and $C \approx 2.44$ mm/N (Figure 3), making it approximately 1.6 times stiffer than scaffold No. 5, due to its concentric ring topology, which distributes bending across closed load paths. Rings acted as springs in series, with three linear radial–circumferential connectors serving as the primary shear-transfer paths, rather than concentrating shear at the base of a single row of protrusions. The displacement gradient decreased from the outer ring towards the center; strain concentrated on the intermediate ring and at the connector junction nodes, and Von Mises stress peaked at these junctions and near the constraints, with nominal values along load-bearing

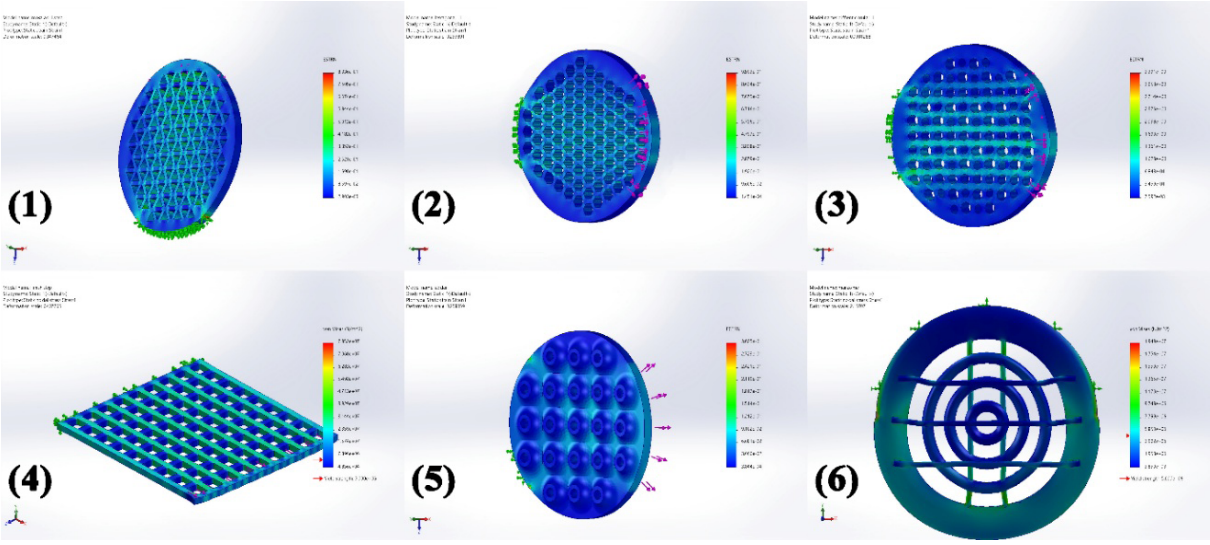

Figure 4. Simulation of the tensile behavior of six scaffolds with different geometric patterns in the simulation environment

members in the tens-of-megapascals range (peaks immediately adjacent to supports being non-governing numerical singularities from idealized contact). Assuming σ_y=5 MPa, these concentrations yielded local FoS less than unity; therefore, modifications including reinforcement of the connector cross-sections and their junction with the intermediate ring, introduction of fillets at connection corners to reduce the stress concentration factor Kt, and provision of a stiffer peripheral ring with even a 20–40% increase in connector width or thickness expected to meaningfully reduce δ and stress concentration, are recommended.

The scaffolds are ranked based on their bending stiffness as follows: No. 3 (k ≈ 5.6 N/mm), No. 1 (k ≈ 4.4 N/mm), No. 2 (k ≈ 4.1 N/mm), No. 6 (k ≈ 0.41 N/mm), No. 4 (k ≈ 0.362 N/mm), and No. 5 (k ≈ 0.26 N/mm). The peak Von Mises stress (σmax) was ≈ 6.1×10^8 Pa for No. 5, ≈ 9.6×10^7 Pa for No. 2, ≈ (2.47–2.53) $\times10^7$ Pa for No. 1, and tens of megapascals for patterns 4 and 6. Since all scaffolds had FoS <1 under current loading and require localized optimization, scaffold No. 3 has the optimal pattern if maximizing stiffness is the sole criterion. Scaffolds No. 1 and No. 2 offer a more pragmatic balance of stiffness and reducible stress peaks (via corner rounding, ring reinforcement, and local mesh refinement), and scaffolds 4 and 5 require a redesign to increase effective moment of inertia for bending applications.

Simulation of scaffolds' tensile behaviors

Figure 4 shows the results of simulating the tensile behaviors of six scaffolds. The tensile load was applied as a distributed force along the upper edge, with the lower edge fully constrained (shown by purple arrows and green constraints). The URES map exhibited a uniform vertical gradient, with the maximum displacement in the upper loaded region reaching approximately $\delta_{max} \approx 11.5$ mm (the deformation scale of approximately 0.35 is for visualization purposes only). Accordingly, the effective tensile stiffness of the structure was approximately ≈ 417.3/11.5 ≈ 36 N/mm. The load path was predominantly transferred from successive rows of triangular webs to the peripheral ring. The cell orientation generates a vertical load-bearing band and a form of tensile anisotropy. The Von Mises stress map reveals a maximum of approximately $\sigma_v M_{max} \approx 1.3\times10^8$ Pa, concentrated primarily along the peripheral ring near the loading region, at the junctions of the triangular webs with the ring, and around the sharp corners of the triangular features. The strain map similarly showed peaks of up to 0.83 in the same regions. Given $\sigma_y \approx 5\times10^6$ Pa (Figure 4), yielding in these sections was possible. Accordingly, to reduce stress concentration and improve tensile capacity, the application of fillets at the triangular corners, reinforcement and thickening of the peripheral ring, and increasing the web width or reducing the pore size in regions proximate to the loading zone are recommended. From a modeling standpoint, owing to the relatively large deformation, activation of the Large Displacement formulation, combined with an elastoplastic material model, where available, and local mesh refinement at the ring and corners would yield more realistic predictions.

In scaffold No. 2, tensile testing under an applied load of F=47.1 N revealed maximum displacement at the loading edge, with the displacement field increasing as a gradient from the constrained edge towards the tensile edge. The maximum displacement (δ_{max}) according to the URES map was approximately 16.1 mm, yielding an effective axial stiffness ($k=F/\delta_{max}$) ≈ 2.9 N/mm. Load paths were observed to pass primarily through the first row of hexagonal cell edges aligned with the tensile axis, concentrating deformation in the columns adjacent to the grips and along the right edge, a pattern corroborated by the strain and stress maps. The highest effective strain localized at the junction ring between the peripheral shell and the first row of cells, as well as around the hexagonal corners aligned with the tensile axis, while the Von Mises stress in these regions reached approximately 1.4×10^{8} Pa, substantially exceeding the defined yield limit (≈5×10^{6} Pa) and indicating that local yielding or necking would likely initiate at these sites. To improve tensile performance, it is recommended to increase the corner radius of cells adjacent to the grips, moderately widen the ligaments in the first column, or incorporate a rigid load-bearing strip (rib or reinforcing edge) at the loading boundary to promote more uniform force transfer and reduce stress concentration.

For scaffold No. 3 under tensile loading of F=425.9 N, the URES map showed the maximum displacement of approximately 42.3 mm near the loaded edge. Accordingly, the effective axial stiffness of the structure was ≈ 425.9/42.31 ≈ 10.1 N/mm. This value is approximately twice the bending stiffness of this scaffold (under F=56 N with a deflection of approximately 10 mm, yielding k ≈ 5.6 N/mm), indicating that this scaffold is considerably stiffer under tension than under bending. The peak strain pattern was concentrated on the diagonal band of large pores and at the free edge on the loading side, reflecting a narrowing of the load path in that region and amplification of stress components around the pore edges (Figure 4). The very high localized strain values near the support and force arrows arise from numerical singularities and idealized contact, and should not serve as a basis for fracture assessment. A more appropriate criterion is the average strain across the load-bearing band, which remains low over most of the surface and can be further reduced by increasing ligament thickness or moving the large-pore band further from the free edge. To improve the tensile response at the same mass, three low-cost modifications are recommended: (i) widening the ligaments in the diagonal large-pore band to create a more continuous load path; (ii) introducing chamfers or small fillets at pore edges to reduce the stress concentration factor; and (iii) local mesh refinement in the diagonal region and at the loading edge to stabilize localized peaks and yield more reliable stress estimates. With the geometry held fixed, a reasonable quantitative goal can be to reduce the displacement of the loaded edge to approximately 30 mm, which can raise the effective stiffness to approximately 14 N/mm and is generally achievable by increasing the ligament width by 30–40% or displacing the large-pore band further inward.

For scaffold No. 4 under tensile loading of F=275 N, the maximum displacement was ≈ 6.60 mm. Accordingly, the effective stiffness was ≈ 275/6.60 ≈ 41.7 N/mm (C= ≈ 0.024 mm/N). The displacement field increased approximately uniformly from the grips toward the loaded edge, with the greatest deformation in the last two element columns (Figure 4). The strain map showed that the horizontal bands near the loaded edge were more active, and larger strain patches were observed at the junctions of horizontal and vertical struts, which constitute the primary load transfer path. Values read from the equivalent strain (ESTRN) map were approximately 0.25–0.35 at the peaks and approximately 0.10–0.18 over the majority of the surface. According to the Von Mises stress map, peaks were concentrated primarily in the same band near the loaded edge and at the internal corners of the junctions (σmax ≈ 25–35 MPa). Given the Yield Strength (σ_y) of 5.0 MPa, the FoS ≈ σ_y/σ_{max} was ≈ 0.14–0.20, which is less than unity, implying a probability of local yielding onset under this loading. Assuming a linear response, the allowable load to maintain stress below yield (F_{allow}) was ≈ 275× ($5/\sigma_{max}$) ≈ 39–55 N. To reduce δ and attenuate stress peaks at the same total structural mass, the most effective modifications include: reinforcing one to two columns near the loaded edge (increasing horizontal strut width or thickness by 20–40%, or adding a peripheral load-bearing frame), introducing fillets at the internal junction corners to reduce stress concentration, and local mesh refinement in the critical zone. A reasonable quantitative goal would be to reduce the edge displacement to ≈ 4 mm, which can raise stiffness to ≈ 69 N/mm.

Under tensile loading (F=548.7 N), scaffold No. 5 showed a uniform displacement gradient yielding δ_{max} ≈ 16.7 mm, k ≈ 32.9 N/mm, and C ≈ 0.030 mm/N, with a Von Mises stress peak (σmax) at ≈ 48.6 MPa in the terminal cell column around the pores and connection fillets. Relative to σ_y=5 MPa, this yields FoS ≈ 0.10 and F_{allow} ≈ 56.5 N, confirming that the response lies outside the linear-elastic range and warrants a geometrically nonlinear reanalysis with plasticity or hyperelasticity. Under F=187.2 N, scaffold No. 6 exhibited better performance (a linear, compliant tensile response) with δ_{max} ≈ 2.16 mm, corresponding to k=F/δ ≈ 86.7 N/mm (C ≈ 0.0115 mm/N), approximately 2.6 times stiffer than scaffold No. 5, due to its concentric-ring topology, which distributes load across multiple closed paths. To narrow

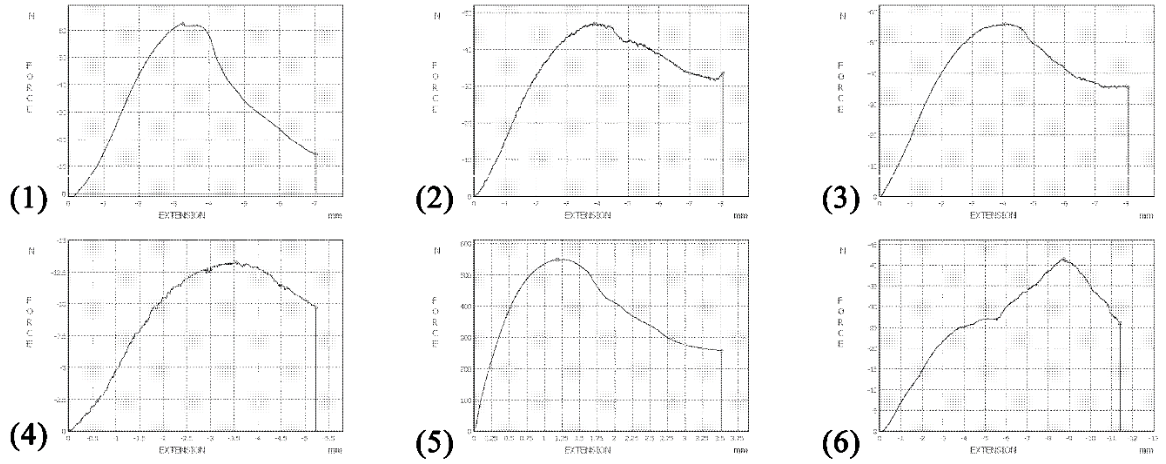

Figure 5. Force-displacement curves for testing the tensile behavior of PCL scaffolds with different patterns

this performance gap, scaffold No. 5 should be modified by distributing the boundary load via an edge strip or reinforcing ring, increasing fillet radius and local thickness around the terminal-column pores, and adding one to two longitudinal ribs from the constrained zone to the first load-bearing cell row, targeting k ≈ 70–90 N/mm. The absorbed strain energy U of scaffold No. 6 was ≈ 1/2 Fδ ≈ 0.20 J. The load was distributed primarily through the peripheral ring and three horizontal struts to the intermediate rings, with the displacement gradient decreasing from edge to center, while effective strain concentrated in the outer ring body and strut connection roots (ranging 0.02–0.06, and peaks near 0.11), confirming this load path. Von Mises stress peaked at ≈ 19.5 MPa at the constraint contact zones and strut bases, giving FoS ≈ σ_y/σ_{max} ≈ 0.26 (σ_y=5 MPa), indicating a possible local yielding; remaining below yield would require roughly quadrupling the cross-sectional area (or thickness) of the outer ring and junction regions, or limiting the load to F_{allow} ≈ 48 N, and reinforcing the outer ring with a continuous peripheral rib, widening or doubling the strut-to-ring connection base, and adding fillets at internal corners could reduce σmax below 1.5 mm and σmax below the yield threshold without added mass.

The scaffolds are ranked based on their tensile stiffness as follows: No. 6 (≈86.7 N/mm), No. 4 (≈41.7 N/mm), No. 1 (≈36 N/mm), No. 5 (≈32.9 N/mm), No. 3 (≈10.1 N/mm), and No. 2 (≈2.9 N/mm). The corresponding stress peak σmax was ≈ 19.5 MPa (FoS ≈ 0.26) for No. 6; ≈ 25–35 MPa (FoS ≈ 0.14–0.20) for No. 4; ≈ 1.3×10^8 Pa (FoS ≈ 0.04) for No. 1; ≈ 48.6 MPa (FoS ≈ 0.10) for No. 5; ≈ 1.4×10^8 Pa (FoS ≈ 0.036) for No. 2, and a moderate stiffness with high localized stresses from notch effects around large pores for No. 3. Since all scaffolds showed FoS <1 and required localized optimization, scaffold No. 6 offers the best stiffness–safety balance, while scaffolds No. 4 and No. 1 forming a secondary tier of adequate stiffness but greater stress concentration.

Experimental testing of tensile behaviors

The experimental tensile test results of the scaffolds (Figure 5) provide a coherent picture of the stiffness and strength hierarchy. Young's modulus (E) and peak failure force were the primary metrics for comparison, both demonstrating that, where load paths were more continuous and geometry-induced stress concentrations decreased, the tensile performance of scaffolds improved considerably. This is consistent with simulation observations. Continuity of the load-bearing path and uniformity of force transfer enhance both the initial slope of the curve and the load-bearing capacity. Quantitatively, scaffold No. 5 exhibited a statistically higher tensile behavior (E ≈ 139.4 MPa, F ≈ 548.7 N), followed by scaffold No. 1 (E ≈ 94.6 MPa, F ≈ 417.3 N), and scaffold No. 3 (E ≈ 77.2 MPa, F ≈ 425.8 N), both offering a favorable balance between stiffness and load-bearing capacity. Scaffolds No. 4 and No. 2 were at the intermediate level (E ≈ 63.6 MPa, F ≈ 275 N) and should be used where larger displacements are acceptable. Scaffold No. 6 exhibited the most compliant response (E ≈ 29.2 MPa, F ≈ 187.2 N) and is better suited for layered or other applications requiring greater flexibility. In terms of curve morphology, stiffer specimens display a steeper initial slope and a higher peak force, whereas the specimens with compliant responses exhibited a shorter quasi-linear region and a lower peak force.

To improve the performance of scaffolds that were at intermediate and lower levels, three low-cost and effec-

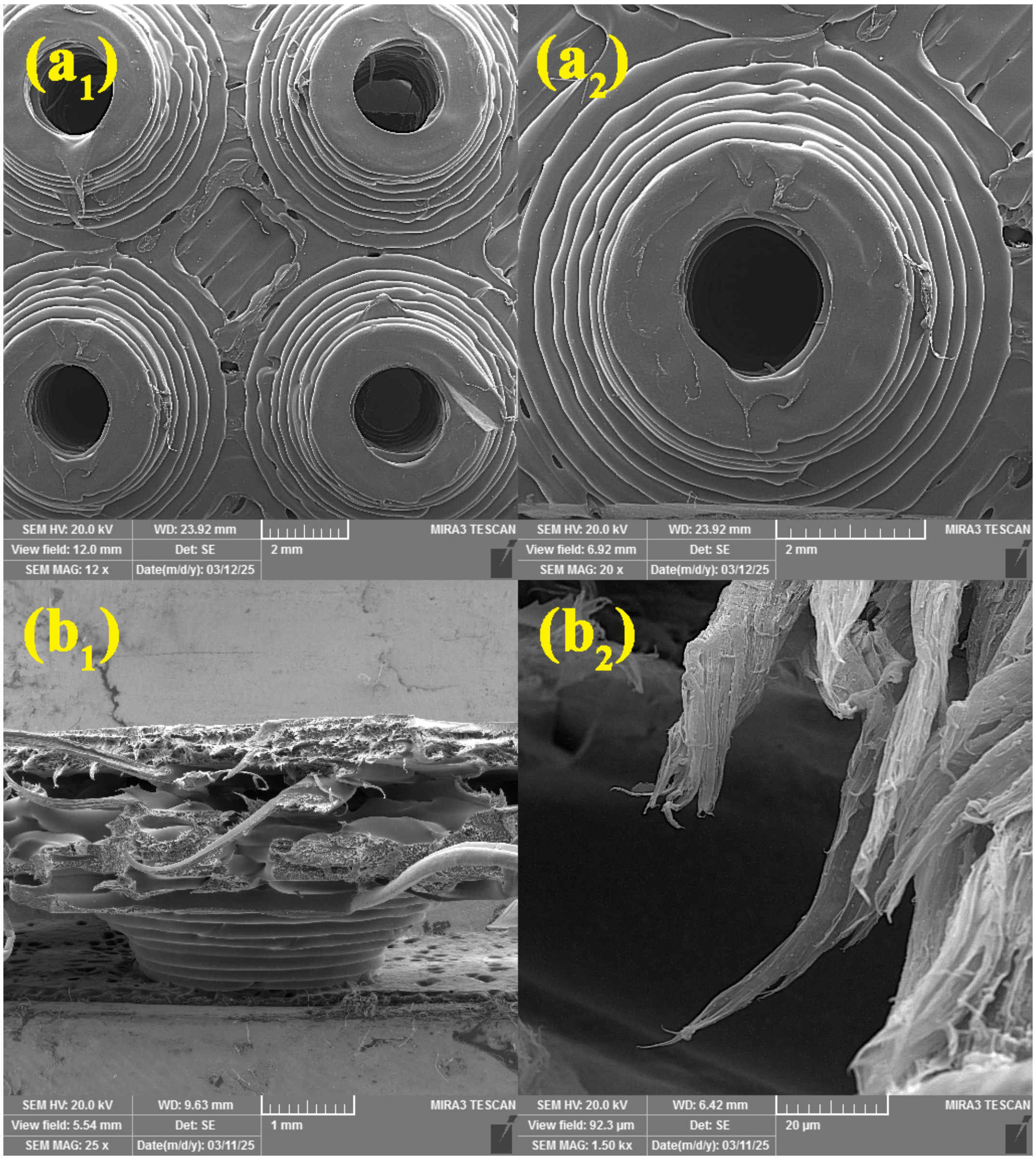

Figure 6. SEM images of the PCL scaffold No. 5

a_1) Top surface view at low magnification showing the periodic arrangement of cylindrical pores and the surrounding filament structure; a_2) surface view at higher magnification revealing the concentric layer-by-layer deposition rings around an individual pore; b_1 and b_2) Cross-sectional view of the fracture surface following tensile testing at various magnifications

tive design methods are recommended: More uniform distribution of the boundary load (by adding a continuous load-bearing edge or ring), increasing the fillet radius around pores and at connection bases to reduce geometry-induced stress concentrations, and locally reinforcing the primary force transfer paths (by increasing thickness or adding low-profile ribs along the load-bearing column). These interventions typically increase the initial slope of the curve (E) and reduce localized stress peaks without a considerable increase in mass, resulting in a higher peak force and improved functional safety.

Figure 6 shows the SEM images of scaffold No. 5 before and after tensile testing. The surface views (Figure 6 a1 and a2) confirmed the geometric regularity of the cylindrical pore arrangement and clearly revealed the concentric filament deposition rings that are characteristic of FDM printing, with no macroscopic discontinuities or void defects apparent in the inter-pore ligaments. The fracture surface images (Figure 6 b1 and b2) showed the morphology of failure following tensile loading. At low magnification, separation along the printed layer interfaces was evident, while at higher magnification,

Table 1. Comparison of compressive stiffness, bending stiffness, and experimental tensile modulus and peak force in scaffolds and their ranks

#	Compressive Stiffness k (Rank)	Bending Stiffness k (Rank)	Exp. E Modulus (Rank)	Exp. F_{peak} (rank)	Selection Score*
1	36 N/mm (2)	4.4 N/mm (2)	94.61 MPa (2)	417.3 N (3)	2.25
2	2.9 N/mm (6)	4.1 N/mm (3)	63.62 MPa (4–5)	275 N (4–5)	5.25
3	11.3 N/mm (4)	5.6 N/mm (1)	77.25 MPa (3)	425.8 N (2)	3.25
4	41.7 N/mm (1)	0.362 N/mm (5)	63.62 MPa (4–5)	275 N (4–5)	2.75
5	33 N/mm (3)	0.26 N/mm (6)	139.49 MPa (1)	548.7 N (1)	2
6	4.22 N/mm (5)	0.41 N/mm (4)	29.19 MPa (6)	187.2 N (6)	5.50

*Selection score=0.5× compressive stiffness rank + 0.5× average of E modulus and F_{peak} ranks.

drawn and elongated polymer features were visible on the fracture surface, reflecting the ductile character of PCL under tensile loading. These observations are generally consistent with the mechanical behavior recorded for this scaffold.

There was agreement between simulation and experimental tensile test results. Both approaches confirmed that continuity of load paths in the vicinity of the loading edge and the peripheral frame is associated with greater stiffness. Accordingly, scaffold No. 1 falls in the upper half of the spectrum in both approaches (k ≈ 36 N/mm in the simulation model and E ≈ 94.6 MPa in the experimental model), and scaffold No. 4 similarly exhibited intermediate-to-high performance. Scaffold No. 3 was at the intermediate level based on both models (k ≈ 10.1 N/mm, E ≈ 77.3 MPa), and the predicted deformation and stress distribution pattern, concentration at ligament junctions and around pores on the loading side, is consistent with the behavior of the experimental model. Furthermore, both approaches demonstrate that patterns with pores proximate to the loading edge and sharp connections were susceptible to stress concentration and premature slope reduction. However, when load was distributed over more continuous paths, a steeper initial slope and higher peak force were recorded. This qualitative agreement in terms of hotspot locations, displacement, and the relative stiffness ratios of scaffolds No. 1 and No. 3 compared to scaffolds provides a sound basis for co-calibration of models with experimental data, and indicates that modifications such as distributing the boundary load and rounding connections, as proposed in the numerical analysis, should also yield improvements in stiffness and reductions in stress concentration under physical testing conditions.

Multi-criteria comparison and selection of the baseline pattern

Table 1 summarizes the structural performance of six scaffolds based on compressive stiffness, bending stiffness, tensile modulus, and peak force. Since the candi-

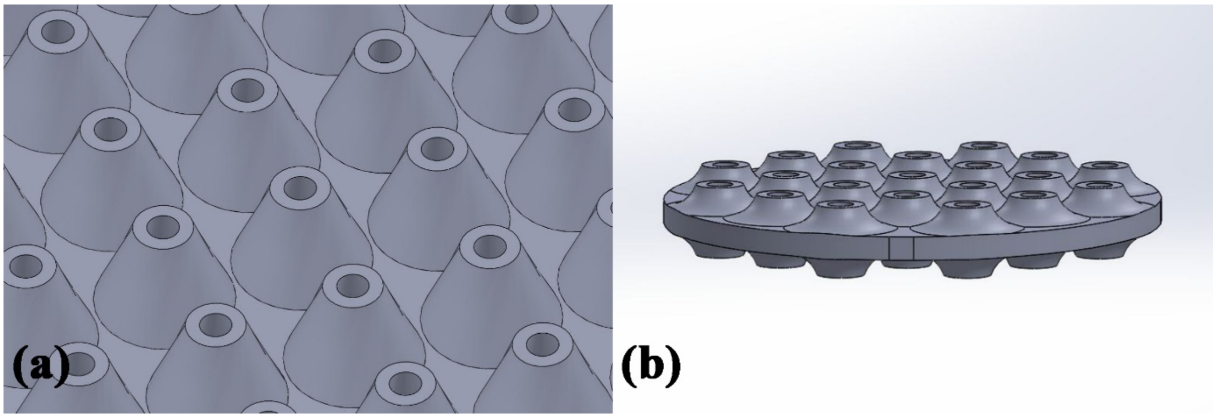

Figure 7. Views of the pore geometry of scaffold No. 5

a) With conical pores, b) With cylindrical pores date scaffold is intended as the subchondral substrate in a layered osteochondral construct where physiological loading is dominated by axial compression and tension rather than bending, the selection criterion combines compressive stiffness and experimental tensile stiffness ranks (average of modulus and peak force ranks) equally. Bending stiffness is reported for completeness but is considered a secondary, locally improvable criterion, not a selection criterion, consistent with its lower physiological relevance to this anatomical region.

Scaffold No. 5 had the lowest (best) composite score, primarily due to its experimentally validated tensile performance, and remained among the top three patterns based on compressive stiffness. Its comparatively low bending stiffness (ranking 6 of 6) is a limitation of the unmodified geometry and is the basis for the localized reinforcement strategies proposed in Section 3.3.

Effect of pore geometry variation in the optimal scaffold

Given that scaffold No. 5 demonstrated superior overall performance and was the optimal pattern among the patterns, it was selected as the design baseline. Subsequently, the effect of pore geometry modification in this scaffold was evaluated to elucidate its mechanical optimization pathway. To this end, the pore geometry was first changed from cylindrical to conical pores, and the effect of this modification was assessed (Figure 7).

After bending the scaffold having cylindrical pores (F=91.3 N), the URES map exhibited a uniform gradient from the fixed edge to the free edge, with the maximum displacement at the free edge reaching ≈ 3.5×10^2 mm. Accordingly, the effective bending stiffness was ≈ 0.26 N/mm. The gradual color distribution shown in the displacement map and the shear–bending band at the transition from the constrained region to the first row of pores indicate that load paths in the cylindrical lattice were relatively continuous, and the constant-thickness ligaments accommodate a greater portion of the bending as axial tension/compression. The stress and strain peaks occurred predominantly around the collar of the first-row pores and at the connection root to the plate, with the Von Mises stress peak of (σmax) ≈ $(5–7)\times10^8$ Pa. Although these peaks substantially exceed σ_y=5 MPa and necessitate localized redesign (larger fillets, reinforcement of the load-bearing ring, and more uniform load distribution), the overall load-bearing path remains predictable, with concentrations confined to the load-bearing band near the loading edge.

In the scaffold with conical pores under the same load, the displacement gradient was steeper, and δ_{max} was considerably larger than in the scaffold with cylindrical pores (color ranges extending to the order of 2.7×10^3 mm in the maps), such that the apparent effective stiffness falls below approximately 0.1 N/mm. The mechanical cause of this stiffness reduction is that the conical pore walls taper toward the apex, diminishing the effective cross-sectional moment of inertia precisely where the tensile and compressive fibers contribute most. Furthermore, the pore base region acts as a geometric bottleneck, amplifying stress peaks. Von Mises peak values of approximately (3.8–4.7) $\times10^9$ Pa were observed around the cone bases and the central transition band. In summary, while both geometries required localized modifications for elastic serviceability, the cylindrical one was the superior geometry for bending applications due to its uniform ligament thickness, more orderly load-bearing path, lower δ_{max}, and reduced stress peaks relative to the conical geometry. If further improvement was required, adding a peripheral rail or frame and increasing the fillet radius around the pores in the load-bearing row of the cylindrical version would simultaneously raise stiffness and suppress concentrations.

Under a tensile force of 548.7 N, the specimen with cylindrical pores was stiffer and showed more uniform behavior. Its URES map showed a continuous gradient from the fixed grip to the free edge, with the maximum displacement of approximately 30 mm, meaning that the overall surface strain was lower. In the strain and stress maps, the high-intensity regions were observed predominantly near the grip zone and the tensile edge, and no continuous weak band formed between the pore rows. In other words, the load was distributed almost evenly among the ligaments surrounding the pores. This more homogeneous strain/stress distribution, along with the absence of pronounced stress concentration at the inner pore ring, reflects a continuous load-bearing path and a lower risk of local yielding or tearing onset. In the specimen with conical pores under the same force, the maximum displacement was larger (approximately 36 mm), indicating a reduction in axial stiffness. Furthermore, the strain and stress maps revealed higher intensity in the half proximate to the tensile edge and around the conical bottlenecks, where the effective ligament cross-section decreased and stress concentration consequently developed. This local thinning accumulates the load at the pore necks rather than distributing it among the surrounding rings, thereby increasing the probability of initiating inelastic deformation or cracking. Therefore, under tension, the cylindrical geometry — with lower displacement, more uniform strain/stress distribution, and a more stable load-bearing path — outperforms the conical geometry and is the preferred scaffold configuration.

Given the demonstrated superiority of the cylindrical pore geometry in most areas, the concept of bilateral pore protrusions (projecting from both sides of the scaffold, rather than one side only) was subsequently investigated. Under compressive loading at F=548.7 N, the bilateral scaffold (protrusions on both sides) exhibited a compressed-edge displacement of approximately 2.2 mm. The strain and stress fields were concentrated primarily in the inter-pore bridges near the loading edge. The maximum strains are observed in the same inter-pore bands, and the maximum Von Mises stress was approximately 4×10^7 Pa (above the 5 MPa yield indicator). These patterns and values did not differ significantly from those of the unilateral specimen. Thus, adding a symmetric protrusion on the second side neither increases the effective stiffness in the compressive direction nor reduces stress concentration around the pore openings and bridges. In fact, due to the reduction in effective cross-section on both faces, it may preserve or slightly intensify the same critical locations. Therefore, in terms of compressive strength and stiffness, the scaffold with a bilateral configuration offers no advantage over the one with a unilateral configuration and merely increases fabrication complexity.

In the simulation of the bilateral specimen's bending behavior (with cylindrical protrusions on both sides), the URES maps exhibited the same general cantilever pattern as in the unilateral specimen (maximum at the free edge), but no stiffness advantage was observed. Contrary to expectation, the strain field (ESTRN), rather than distributing across the outer surfaces, concentrated as a narrow, continuous band along the region where the opposing protrusions were in closest proximity; that is, a hinge-like line formed in the intermediate web. The Von Mises stress maps corroborated this concentration, showing higher peaks within this band and near the pore edges than in the unilateral specimen. In other words, making the pores bilateral not only fails to distribute stress but also creates a preferential stress-concentration path. The mechanical cause of this behavior is that the bilateral protrusions, rather than adding a continuous outward flange distal from the neutral axis (which would increase the section's moment of inertia), are positioned directly opposite one another, leaving a thin neck between them. This intermediate neck enters membrane deformation earlier under bending and becomes the dominant locus of strain and stress. Therefore, the bilateral configuration offers no significant bending advantage over the unilateral configuration and, considering its elevated stress peaks, it even reduces the safety. As a result, the unilateral cylindrical configuration is the more appropriate choice for testing bending behavior. If bilateral pores are mandated, the intermediate web thickness should be increased, or the protrusions on the two sides should be arranged in a staggered (non-opposing) pattern with appropriately rounded fillets to reduce stress concentration.

Under tension, the bilateral specimen's displacement field exhibited a uniform, stepwise progression from the constrained edge toward the tensile edge, with the maximum displacement at the loading edge of approximately 2.2 mm. The strain and Von Mises stress maps indicated that the primary concentration formed at the load-bearing necks between pores and along the load path (inter-pore columns), not on the protrusions themselves. The peak stress values in the bilateral specimen were also in the range of tens of megapascals ($\approx 4\times10^7$ Pa), and the stress/strain bands were formed approximately as strips within the mid-layer of the inter-pore web, meaning that the tensile behavior remains ligament-dominated and the bilateral protrusions do not meaningfully distribute stress through the thickness.

Comparison with the unilateral cylindrical specimen revealed that the field patterns were essentially identical. The maximum deformation and stress occurred at the same load-bearing necks, and differences in peak values were on the order of a few tens of percent, with no qualitative change in the load-bearing path. In mechanical terms, the governing parameter in tensile loading was the effective cross-sectional area of the ligaments in the loading direction. Adding protrusions on the opposite side, provided that it does not increase the net ligament's cross-section or is not accompanied by a significant increase in overall mass or thickness, confers no reliable advantage. Therefore, in terms of both stiffness (displacement) and strength, the bilateral specimen demonstrates no considerable superiority over the unilateral specimen under tension, and even accounting for the greater fabrication complexity and mass, no clear mechanical justification exists for its selection.

Discussion

The numerical analyses and experimental tests demonstrated that the selection of an appropriate geometry and the arrangement of load paths within the PCL scaffolds were important factors in making them suitable for osteochondral regeneration. Under tensile force, scaffold No. 5 had the best performance with E ≈ 139.49 MPa and $F_{peak} \approx 548.7$ N, followed by scaffold No. 1 (E: ≈

94.61 MPa, F_{peak}: ≈ 417.3 N) and scaffold No. 3 (E: ≈ 77.25 MPa, F_{peak}: ≈ 425.8 N). Scaffolds No. 2 and No. 4 were in the intermediate rank (E ≈ 63.62 MPa, F_{peak} ≈ 275 N), while scaffold No.6 was in the lowest rank (E ≈ 29.19 MPa, F_{peak} ≈ 187.2 N). This stiffness–strength spectrum is consistent with the stress and strain field patterns predicted by numerical simulation and enables a functional mapping. Scaffold No. 5 was most suitable for the subchondral bone substrate and regions requiring firm mechanical support; scaffold No. 1 for the subchondral zone; scaffold No. 3 for the osteochondral transition region; scaffolds No. 2 and No. 4 for the deep/calcified cartilage layer; and scaffold No. 6 for the soft cartilaginous layer.

Under compressive force, both numerical and experimental results confirmed that stiffer specimens (scaffolds No. 5 and No. 1) provided better initial mechanical support and more closely satisfied subchondral requirements, while the specimens with compliant responses were advantageous for cartilaginous regions where greater displacement is acceptable [15-17].

Almost in all scaffolds and loadings, simulated peak Von Mises stresses substantially exceeded the assumed PCL yield strength of 5 MPa, with low computed FoS ~0.008–0.26 in several scaffolds. This reflects that the applied simulation loads were set to match the experimentally observed peak fracture forces. When local stresses exceed yield, a linear-elastic solver cannot capture plastic flow, stress redistribution, or strain hardening, nor the geometric effects of large local deformation; therefore, the absolute magnitude of these peak stresses should not be taken as a precise quantitative measure of failure prediction. The relative comparisons among the scaffolds, however, remained considerable, since identical constitutive assumptions and boundary conditions were applied uniformly across all six geometries. The numerical stiffness ranking and the locations of stress concentrations (sharp corners, pore necks, ligament junctions) were expected to be robust to this simplification, as supported by the close qualitative agreement between the numerically predicted stiffness ranking and the experimentally measured tensile stiffness and strength rankings. Future work should incorporate an elastoplastic constitutive model, parameterized directly from the full experimental stress–strain curves obtained in this study, together with a geometrically nonlinear formulation, to enable quantitatively accurate prediction of post-yield stress fields and failure loads.

The mechanical properties of PCL scaffolds obtained in this study are consistent with previously reported values for FDM-printed PCL scaffolds. Hutmacher et al. reported a compressive stiffness of 41.9±3.5 MPa and a 1% offset yield strength of 3.1±0.1 MPa for a honeycomb-pattern PCL scaffold with a 0/60/120 lay-down pattern, while Zein et al. reported compressive stiffness ranging from 4 to 77 MPa and yield strength from 0.4 to 3.6 MPa across a porosity range of 48 to 77% for similarly fabricated honeycomb PCL scaffolds [18, 19]. The 5 MPa yield strength assumed in the finite element models of this study falls within their reported range, supporting its use as the failure criterion. Yazdanpanah et al. reported elastic moduli of 14-165 MPa and yield strengths of 0.9-10 MPa for 3D-printed PCL/nano-hydroxyapatite scaffolds designed to mimic trabecular bone [20], a range that brackets the experimentally measured tensile moduli obtained in this study (29.19-139.49 MPa across six scaffolds) despite the absence of ceramic reinforcement, indicating that pore geometry optimization alone can cause unreinforced PCL scaffolds to enter a stiffness range, otherwise it is associated with composite formulations.

From the perspective of pore geometry design, the results of bending and tensile tests indicated that unilateral cylindrical pores produce a more uniform displacement field, lower maximum displacement (δ_{max}), and more limited stress concentration compared to the bilateral or conical pores. The addition of a symmetric protrusion on the second side, without increasing the effective cross-sectional area of the load-bearing paths, neither significantly raised stiffness nor reduced peak stresses at the necks of the inter-pore bridges. Accordingly, for osteochondral regeneration applications, the proposed design pathway is to retain the unilateral cylindrical geometry and refine it through localized modifications: more uniform distribution of the boundary load via a peripheral rail or frame, increasing the fillet radius around the load-bearing pores, reinforcing the critical band between the constrained strip and the first row of cells, and adjusting the pore pitch and diameter to balance stiffness and permeability. This approach simultaneously satisfies the requirements of physiological mechanotransduction, permeability, and structural integrity while, due to its fabrication simplicity, maintaining low risk of production heterogeneity and manufacturing defects. The cyclic fatigue evaluation under quasi-physiological loading conditions can further verify the in vivo durability of the proposed design [21-24]. Experimental verification in this study was limited to tensile loading; compressive and bending simulations were not independently tested against experimental results. Future work should include compressive and three-point bending tests on the candidate patterns to verify the simulated stiffness and stress trends under these loading modes.

This study was limited to the mechanical and structural characterization of the 3D printed PCL scaffolds. Biological evaluation, hydrolytic or enzymatic degradation testing, and cyclic fatigue testing under physiological loading were not performed. These are acknowledged as necessary next steps before any claim of biological or clinical applicability can be made, and the findings should be interpreted as a mechanical design and screening framework for PCL scaffold geometry. For more accurate assessment closer to experimental conditions, it is recommended that geometric nonlinearity and, where necessary, material models beyond linear elasticity be incorporated into the analysis, and that cyclic fatigue tests be conducted.

Conclusion

The qualitative agreement between numerical and experimental results demonstrates that the optimal design strategy for PCL scaffolds is the unilateral cylindrical geometry, and that a focus should be on localized improvements: reinforcing the load-bearing frame and edges, increasing the fillet radius at connections, and making load application more uniform. Bilateral configuration and conical pores offer no stability advantage, as they generate stress concentration bands and reduce the effective moment of inertia. These findings provide a practical framework for the purposeful design of layered scaffolds and for tailoring the mechanical response to meet the specific requirements of tissue repair.

Ethical Considerations

Compliance with ethical guidelines

There were no ethical considerations to be considered in this research.

Funding

This research did not receive any grant from funding agencies in the public, commercial, or non-profit sectors.

Authors' contributions

Conceptualization and writing: Hosein Rostamani and Omid Fakhraei; Methodology: Hediye Paranion and Anahita Mousazadeh Moghaddam; Data analysis: Mohammad Javad Khosravi; Investigation: Mohammad Javad Khosravi, Hediye Paranion and Anahita Mousazadeh.

Conflict of interest

The authors declared no conflict of interest.

Acknowledgments

The authors wish to express their gratitude to Shahryar Salmani Bajestani for his valuable assistance.

References

[1] Wang C, Huang W, Zhou Y, He L, He Z, Chen Z, et al. 3D printing of bone tissue engineering scaffolds. Bioactive Materials. 2020; 5(1):82-91. [DOI:10.1016/j.bioactmat.2020.01.004] [PMID]

[2] Rahmati M, Mills DK, Urbanska AM, Saeb MR, Venugopal JR, Ramakrishna S, et al. Electrospinning for tissue engineering applications. Progress in Materials Science. 2021; 117:100721. [DOI:10.1016/j.pmatsci.2020.100721]

[3] Yang X, Wang Y, Zhou Y, Chen J, Wan Q. The application of polycaprolactone in three-dimensional printing scaffolds for bone tissue engineering. Polymers. 2021; 13(16):2754. [DOI:10.3390/polym13162754] [PMID]

[4] Mabrouk M, Beherei HH, Das DB. Recent progress in the fabrication techniques of 3D scaffolds for tissue engineering. Materials Science & Engineering. C, Materials for Biological Applications. 2020; 110:110716. [DOI:10.1016/j.msec.2020.110716] [PMID]

[5] Joseph B, James J, Grohens Y, Kalarikkal N, Thomas S. Additive manufacturing of poly (ε-caprolactone) for tissue engineering. JOM. 2020; 72(11):4127-38. [DOI:10.1007/s11837-020-04382-3]

[6] Hou Y, Wang W, Bartolo P. Investigation of polycaprolactone for bone tissue engineering scaffolds: In vitro degradation and biological studies. Materials & Design. 2022; 216:110582. [DOI:10.1016/j.matdes.2022.110582]

[7] Zhang F, King MW. Biodegradable polymers as the pivotal player in the design of tissue engineering scaffolds. Advanced Healthcare Materials. 2020; 9(13):1901358. [DOI:10.1002/adhm.201901358] [PMID]

[8] Shen J, Yuan W, Badv M, Moshaverinia A, Weiss PS. Modified poly (ε-caprolactone) with tunable degradability and improved biofunctionality for regenerative medicine. ACS Materials Au. 2023; 3(5):540-7. [DOI:10.1021/acsmaterialsau.3c00027] [PMID]

[9] Rostamani H, Fakhraei O, Kelidari N, Toosizadeh Khorasani F. Improving biological and mechanical properties of bioprinted PCL-alginate-chondrocyte scaffolds for patellofemoral cartilage tissue regeneration. Journal of Biomaterials Science, Polymer Edition. 2024; 35(16):2549-69. [DOI:10.1080/09205063.2024.2385182] [PMID]

[10] Fakhraei O, Rostamani H, Aliebrahim Nosh Abad A, Valizadeh S, Bakhshayeshi MM, Rafienia M. Enhanced biological properties of polyvinyl alcohol-polycaprolactone/hyaluronic acid-coated electrospun scaffolds for articular cartilage regeneration. Journal of Biomaterials Science. Polymer Edition. 2025; 36(15):2187-215. [DOI:10.1080/09205063.2025.2492462] [PMID]

[11] Rostamani H, Fakhraei O, Toosizadeh Khorasani F, Kelidari N. [A review of 3D bioprinting technologies in the reconstruction of human nasal cartilaginous tissue (Persian)]. Journal of Guilan University of Medical Sciences. 2024; 33(2):134-59. [DOI:10.32598/JGUMS.33.2.2574.1]

[12] Fakhraei O, Hesaraki S, Alizadeh M. Evaluation of biphasic calcium phosphate/nanosized 3YSZ composites as toughened materials for bone substitution. Ceramics International. 2016; 42(9):11201-8. [DOI:10.1016/j.ceramint.2016.04.030]

[13] Beșliu-Băncescu I, Tamașag I, Slătineanu L. Influence of 3D printing conditions on some physical-mechanical and technological properties of PCL wood-based polymer parts manufactured by FDM. Polymers. 2023; 15(10):2305. [DOI:10.3390/polym15102305] [PMID]

[14] Koch F, Thaden O, Conrad S, Tröndle K, Finkenzeller G, Zengerle R, et al. Mechanical properties of polycaprolactone (PCL) scaffolds for hybrid 3D-bioprinting with alginate-gelatin hydrogel. Journal of The Mechanical Behavior of Biomedical Materials. 2022; 130:105219. [DOI:10.1016/j.jmbbm.2022.105219] [PMID]

[15] Fakhraei O, Hesaraki S, Alizadeh M. Fracture toughness and R-curve behavior of BCP/YTZP nanocomposites produced using the spark plasma sintering process. Journal of Alloys and Compounds. 2017; 725:623-31. [DOI:10.1016/j.jallcom.2017.07.194]

[16] Rostamani H, Fakhraei O, Zamirinadaf N, Mahjour M. An overview of nasal cartilage bioprinting: from bench to bedside. Journal of Biomaterials Science, Polymer Edition. 2024; 35(8):1273-320. [DOI:10.1080/09205063.2024.2321636] [PMID]

[17] Radhakrishnan S, Nagarajan S, Belaid H, Farha C, Iatsunskyi I, Coy E, et al. Fabrication of 3D printed antimicrobial polycaprolactone scaffolds for tissue engineering applications. Materials Science & Engineering. C, Materials for Biological Applications. 2021; 118:111525. [DOI:10.1016/j.msec.2020.111525] [PMID]

[18] Borhan S, Hesaraki S, Shahrezaee M. Evaluation of 3D printed polycaprolactone/tetracalcium phosphate nanocomposite as potential scaffold for bone tissue engineering. Journal of Materials Research and Technology. 2025; 36:1130-45. [DOI:10.1016/j.jmrt.2025.03.098]

[19] Hesaraki S, Saba G, Shahrezaee M, Nezafati N, Orshesh Z, Roshanfar F, et al. Reinforcing β-tricalcium phosphate scaffolds for potential applications in bone tissue engineering: Impact of functionalized multi-walled carbon nanotubes. Scientific Reports. 2024; 14(1):19055. [DOI:10.1038/s41598-024-68419-2] [PMID]

[20] Xu Z, Omar AM, Bartolo P. Experimental and numerical simulations of 3D-printed polycaprolactone scaffolds for bone tissue engineering applications. Materials. 2021; 14(13):3546. [DOI:10.3390/ma14133546] [PMID]

[21] Zein I, Hutmacher DW, Tan KC, Teoh SH. Fused deposition modeling of novel scaffold architectures for tissue engineering applications. Biomaterials. 2002; 23(4):1169-85. [DOI:10.1016/S0142-9612(01)00232-0] [PMID]

[22] Hutmacher DW, Schantz T, Zein I, Ng KW, Teoh SH, Tan KC. Mechanical properties and cell cultural response of polycaprolactone scaffolds designed and fabricated via fused deposition modeling. Journal of Biomedical Materials Research. 2001; 55(2):203-16. [DOI:10.1002/1097-4636(200105)55:23.0.CO;2-7] [PMID]

[23] Yazdanpanah Z, Sharma NK, Raquin A, Cooper DML, Chen X, Johnston JD. Printing tissue-engineered scaffolds made of polycaprolactone and nano-hydroxyapatite with mechanical properties appropriate for trabecular bone substitutes. BioMedical Engineering OnLine. 2023; 22(1):73. [DOI:10.1186/s12938-023-01135-6] [PMID]

[24] Rostamani H, Firouzfar S, Fakhraei O, Nakhaei N, Shahraki N, Rafienia M. Dual-functionalized electrospun PLA/PCL blend scaffolds as bioactive platforms for osteochondral tissue engineering. International Journal of Polymeric Materials and Polymeric Biomaterials. 2026; 75:(11-14):1389-405. [DOI:10.1080/00914037.2026.2690024]